Materials Advances

ROYAL SOCIETY OF CHEMISTRY

PAPER

View Article Online
View Journal

Cite this: DOI: 10.1039/d6ma00494f

Controlling optoelectronic properties of carbazole-pyridinium luminophores *via* kinetic polymorphism

Roman Viter, *[a] Matiss Martins Drava,[b] Alice Sciortino, [c] Mahmoud Abid,[d] Viktor Zabolotnii,[a] Marco Cannas, [c] Mikhael Bechelany [d] and Artis Kinens *[be]

This study demonstrates the use of kinetic polymorphism to modulate the optoelectronic properties of the donor–acceptor luminophore KL1421 without chemical modification. By employing a swift precipitation method, we selectively isolated three distinct polymorphs arising from specific rotational conformers of the pyridinium subunit, as confirmed by structural and vibrational analysis. These structural variations result in tunable band gaps (2.80–2.95 eV) and high solid-state quantum yields (61–80%), where geometric constraints on the donor–acceptor twist angle directly influence HOMO–LUMO overlap. Furthermore, temperature-dependent photoluminescence reveals that out-of-plane pyridinium rotamers, which restrict π–π^+ interactions, promote thermally activated non-radiative transitions *via* triplet traps, distinguishing the mechanism from delayed fluorescence and highlighting the potential of kinetic control for tailoring functional organic materials.

Received 8th April 2026,
Accepted 1st June 2026

DOI: 10.1039/d6ma00494f

rsc.li/materials-advances

1. Introduction

Organic luminescent materials have garnered immense attention in recent years for their applications in optoelectronic devices, sensors, and optical memory.[1] Among these, donor–acceptor (D–A) type molecules based on carbazole derivatives are particularly prominent due to their high thermal stability, excellent hole-transporting mobility, and tunable photophysical properties.[2] A critical challenge in the development of these materials is overcoming aggregation-caused quenching (ACQ), a phenomenon common in planar aromatic systems.[3] To address this, the design of aggregation-induced emission (AIE) luminogens has emerged as a powerful strategy, often achieved by introducing twisted molecular conformations that restrict intramolecular motion (RIM) and prevent detrimental π–π stacking in the solid state.[4] In carbazole-based donor–acceptor systems, controlling the dihedral twist angle is conventionally used to minimize the singlet–triplet energy gap to facilitate thermally activated delayed fluorescence (TADF), although recent findings show that stable intramolecular charge-transfer states can also be achieved in co-planar rigidified structures.[5]

While chemical modification is the standard approach to tuning optoelectronic properties, polymorphism offers a compelling alternative, allowing for the modulation of emission color and quantum yield without altering the molecular formula.[6] The optical properties of solid-state fluorophores are dictated not just by individual molecular structure, but by molecular packing and intermolecular interactions, including hydrogen bonding and dipole–dipole interactions within the crystal lattice.[7] Consequently, controlling the crystallization process to access specific polymorphs is of great interest. Recent studies have demonstrated that parameters such as solvent choice, supersaturation levels, and cooling rates are decisive in selectively nucleating thermodynamically stable or kinetically trapped metastable polymorphs.[8] For instance, swift cooling crystallization has been successfully employed to isolate distinct polymorphs by generating high supersaturation, thereby bypassing the formation of the most stable crystal phase.[9]

Pyridinium salts attached to carbazole donors represent a fascinating class of AIEgens where the emission is highly sensitive to the local environment and the nature of the counterion.[10] The electrostatic interactions between the cationic pyridinium core and its counterion can significantly influence molecular planarity and packing, yet the specific role of

[a] Institute of Atomic Physics and Spectroscopy, Faculty of Exact Sciences and Technologies, University of Latvia, Jelgavas street 3, Riga, LV 1004, Latvia. E-mail: roman.viter@lu.lv
[b] Faculty of Medicine and Life Sciences, University of Latvia, Jelgavas street 1, Riga, LV 1004, Latvia. E-mail: artis.kinens@lu.lv
[c] Physics and Chemistry Department - Emilio Segrè, University of Palermo, via archirafi 36, 90123, Palermo, Italy
[d] Institut Européen des Membranes, IEM, UMR 5635, University of Montpellier, ENSCM, CNRS, Montpellier, France
[e] Latvian Institute of Organic Synthesis, Aizkraukles street 21, LV-1006, Riga, Latvia

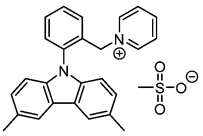

Fig. 1 Chemical structure of carbazole-pyridinium luminophore.

conformational rotamers in these ionic systems remains underexplored.[11]

Previously, we have reported on the successful synthesis and investigation of the structure and optical properties of carbazole-pyridinium luminophore, KL1421 (Fig. 1).[12,13] The theoretical modelling of the interaction between the surface of KL1421 and volatile compounds such as acetic acid, ammonia, and water has been investigated. It was shown that theoretical modelling didn't fit well with experimental results due to limitations of modelling and the significant role of the bulk-surface interface in KL1421. KL1421 showed a high quantum yield (80%) and significant chemical stability in a basic environment. Due to the advanced properties of KL1421, this new material has potential in functional coatings, sensors, and custom-formulated inks. The properties of the final product, formulated from KL1421, could differ from the properties of the as-prepared powder due to deposition and drying conditions. The role of recrystallization from solution of KL1421 has not been investigated yet, and it plays an important role in future applications of novel pyridinium luminophores.

In this work, we investigate the polymorphism of a carbazole-pyridinium luminophore, KL1421, and report the selective isolation of three distinct polymorphs (A, B, and C) *via* a swift precipitation strategy. By leveraging the temperature dependence of photoluminescence, X-ray diffraction (XRD), Raman spectroscopy, optical spectroscopy, X-ray photoelectron spectroscopy (XPS), vibrational spectroscopy (FTIR), and density functional theory (DFT) calculations, we elucidate the conformation-optical properties relationship of polymorphs. We demonstrate that the distinct optical band gaps (ranging from 2.80 to 2.95 eV) and high quantum yields (61–80%) of these forms arise from specific rotational conformers of the pyridinium subunit relative to the carbazole core, stabilized by the orientation of the mesylate counterion. This study demonstrates how kinetic control during crystallization can be utilized to fine-tune the optoelectronic properties of ionic organic luminophores.

2. Experimental part

2.1. Preparation of polymorphs

2.1.1. Polymorph A. The luminophore KL1421 (50.0 mg, 0.11 mmol) was dissolved in MeCN (1.30 mL). To this yellow solution, Et_2O (10.0 mL) was added in a single portion. The white precipitates were washed with Et_2O (5.00 mL), transferred to a glass vial (10.0 mL), and dried under reduced pressure for 30 min.

2.1.2. Polymorph B. The luminophore KL1421 (50.0 mg, 0.11 mmol) was dissolved in MeCN (1.30 mL). To this yellow solution, Et_2O (10.0 mL) was added dropwise at a rate of one drop of Et_2O every 2 s. During the addition, the flask was gently swirled. The light green precipitates were washed with Et_2O (5.00 mL), transferred to a glass vial (10.0 mL), and dried under reduced pressure for 30 min.

2.1.3. Polymorph C. The luminophore KL1421 (50.0 mg, 0.11 mmol) was dissolved in MeCN (2.60 mL). To this yellow solution, methyl *tert*-butyl ether (10.0 mL) was added in a single portion. The white precipitates were washed with methyl *tert*-butyl ether (5.00 mL), transferred to a glass vial (10.0 mL), and dried under reduced pressure for 30 min.

2.2. Characterization

2.2.1. Sample preparation. The polymorphs were prepared and studied in powder form. Five milligrams of the powder were selected for each experiment, described in Sessions 2.3.2–2.3.4. For instance, the powder samples have been deposited into a sample holder with a cylindrical cavity of 0.7 cm in diameter and 0.5 mm in depth. Thin powder layers with homogeneous surfaces have been achieved. After adsorption tests and optical characterization, the powders were transferred into specific holders and vials for NMR, XRD, and FTIR measurements.

2.2.2. Structure and optical properties. The structural properties of the polymorphs were studied by XRD (Bruker D8 diffractometer, CuKa radiation, Germany) and FTIR (ATR mode, Bruker II Alfa, Germany).

Optical properties of the luminophore have been studied by diffuse reflectance spectroscopy and photoluminescence in the UV-Visible range. Ocean Optics fiber optic light source (DH2000, 250–900 nm, USA), integrating sphere (Ocean Optics, IS-8, USA), and fiber optic spectrometer (Ocean Optics HR4000, USA) have been used to record diffuse reflectance spectra.

Excitation of photoluminescence and Quantum Yield of the photoluminescence have been measured by using FS5 spectrofluorometer (Edinburgh Instruments, Livingston, Scotland), equipped with plug-in integrating-sphere sample module SC-30 (150 mm internal sphere diameter). Three measurements have been performed to obtain average values of the excitation spectra and the Quantum Yield.

Photoluminescence of the luminophore has been excited by a UV LED at 310 nm. The excitation power of the LED varied from 0.068 mW to 0.6 mW. The photoluminescence spectra were recorded by a fiber optic spectrometer (Ocean Optics HR4000, USA). The temperature dependence of photoluminescence was measured in a cryostat Linkam 600TMS (Surrey, UK) with a constant heating speed of 50 °C min^{-1}.

Time-resolved photoluminescence measurements were recorded on an intensified charge-coupled device (CCD) camera while exciting the sample by a tunable laser system consisting of an optical parametric oscillator pumped by a Q-switched Nd:YAG laser (5 ns pulses at 10 Hz repetition rate). The energy of laser pulses was about 0.1 mJ, and the spectral resolution is 4 nm (guaranteed by using an appropriate monochromator and a slit). The CCD camera records the emission spectra after variable delays with respect to laser pulses in a fixed time

window of 10 ns. The excitation wavelength has been fixed at 310 nm. The decay kinetics of the fluorescence was measured by extracting the time dependence of the spectrally-integrated emission intensity and the decay curves were least-squares fitted to a single exponential fitting function ($I(t) = A^* \exp(-t/t)$) or a bi-exponential fitting function ($I(t) = A^* \exp(-t/t_1) + B^* \exp(-t/t_2)$). The accuracy of the lifetime value is about 1 ns.

3. Results

3.1. Structural properties

Differential scanning calorimetry (DSC) spectra of the polymorphous luminophores are shown in Fig. 2a. The DSC curves showed an endothermic peak at 272 °C, corresponding to the melting peak.[14] Based on the DSC calculations,[15] we have calculated the characteristic glass transition temperature (T_g) and melting temperature (T_m). The data are collected in Table 1. The T_g and T_m values of the polymorphs A–C show that a slight decrease in the T_g and T_m was found for polymorphs A and C, compared to polymorph B.

XRD spectra of the prepared KL1421 polymorphic materials are shown in Fig. 2b. All KL1421 polymorphs showed good crystallinity. The method of precipitation significantly changed the crystalline structure of the polymorphs. Based on the data reported in our previous work, we assume that KL1421 has a triclinic structure.[12] Using numerical simulations for triclinic crystalline structure and the lattice parameters data reported by Leduskrasts.[13] We calculate (*hkl*) indexes of the planes with the following data, presented in Table 1.

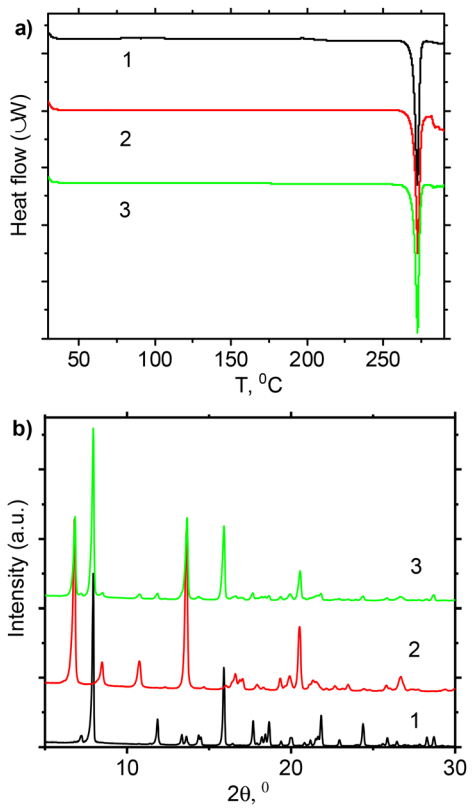

Fig. 2 Thermal and structural characterization of polymorphous luminophores KL1421 A–C (1-A. 2-B, 3-C) by using DSC measurements (a) and XRD measurements (b).

Main orientations of the KL1421 crystalline lattice,[12] were (001), (002), (030). According to XRD spectra, polymorph B, fabricated with the same procedure parameters, fits well with the previously reported data. Deviation in the drying procedure results in recrystallization and rearrangement of the crystalline structure along (01−1) and (012) directions.

Raman and FTIR spectra of the polymorphous materials are shown in Fig. 3. In the literature, Raman peaks of pyridinium compounds could be split into several groups (Table S2 in SI).

Comparative analysis of the Raman spectra of polymorphs A–C showed the following differences:[16–20]

- change in Py skeleton vibrations at 80–150 cm^{-1};
- change of peak intensities, corresponding to δC–H bending vibrations 778, 940, 959 cm^{-1} or/and S–O mesylate ion vibrations 946 cm^{-1};
- change of peak intensities, corresponding to CH_2/CH_3 alkyl vibrations, C–O, COO–, C═O 1000–1650 cm^{-1} or/and S═O mesylate vibrations 1081 cm^{-1};
- new peaks for polymorphs B, C at 300–700 cm^{-1}, related to C–H and N–H stretching.

As no new strong Raman peaks have been observed under transition from polymorph A to polymorph C, we consider that changes in Raman spectra of the polymorphous materials correspond to changes in crystalline structure and enhancement/quenching of the specific molecular vibrations in the luminophore structure.

FTIR spectra of the polymorphous luminophores are shown in Fig. 3b. Based on the FTIR spectra analysis of KL1421 luminophores, reported by Zabolotnii *et al.*,[12] we apply the same analysis for the polymorphic changes. We can identify several groups of the FTIR peaks:[21]

- 3200–3000 cm^{-1} peaks from (methyl)pyridinium ion;
- 2900–2800 cm^{-1} C–H (sp^3 hybridization) and C═C (sp^2 hybridization;[12]
- 1650–1300 cm^{-1} peaks from pyridinium ion and carbazole group;
- 1250–1000 cm^{-1} peaks mostly from pyridinium ion and mesylate ion.

Table 1 Characteristic parameters, calculated from DSC and XRD data

Polymorph	T_g, °C	T_m, °C	XRD peak positions and crystalline orientations
A	269.71	272.50	7.93 (01−1), 11.85 (na), 13.34 (002), 13.61 (020), 14.31 (200), 14.49 (111), 15.88 (012), 17.66 (201), 18.15(21−2), 18.40 (−212), 18.65 (2−21), 20.00 (112), 20.76 (030), 21.17 (300), 21.82 (202), 22.94 (013), 24.38 (na), 25.86 (113)
B	270.10	272.85	6.78 (001), 8.47 (−101), 10.73 (011), 13.76 (002), 16.62 (012), 17.04 (201), 19.92 (112), 20.55 (030), 21.34 (300), 26.66 (311)
C	269.87	272.66	6.78 (001), 7.94 (01−1), 13.65 (002), 15.93 (012), 20.57 (030).

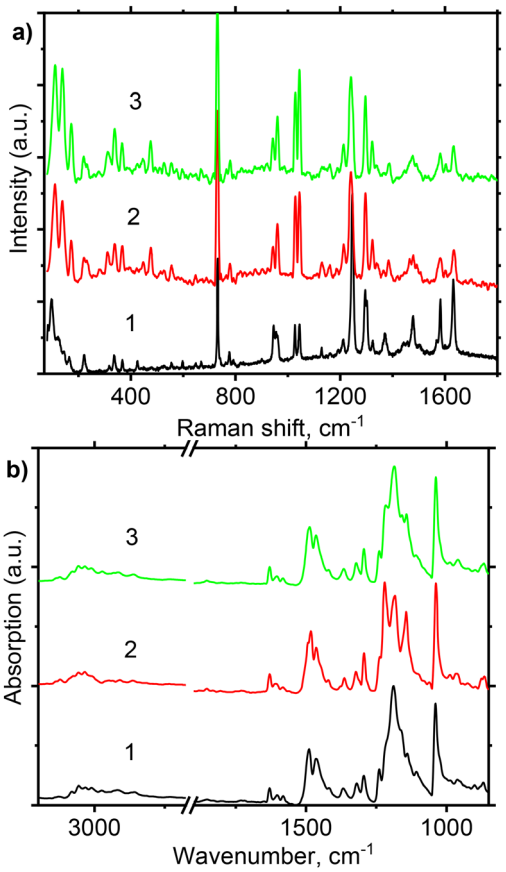

Fig. 3 Structural properties of polymorphous luminophores KL1421 A–C (1-A. 2-B, 3-C) were investigated by Raman (a) and FTIR spectroscopy (b).

Importantly, S═O stretching vibrations, characteristic of mesylate ion ($CH_3SO_3^-$), typically appear in the 1100–1300 cm^{-1} region.[22–24]

Comparative analysis of the FTIR spectra of polymorphs A–C showed peaks with intensities in the range of 3100–3000 cm^{-1}, 2900–2800 cm^{-1}, and 1700–1300 cm^{-1}. Shift of the peak position has been observed for the peak located at 1494 cm^{-1} (polymorph C). The most significant changes have been observed in the region 1291–1054 cm^{-1}. At first sight, the FTIR spectra have been significantly changed from polymorph A to polymorph C, demonstrating a new peak shape. The detailed analysis showed no new peaks that appeared in the range of 1291–1054 cm^{-1}, with the only strong distribution of the intensity of the individual peaks. Based on the peak description provided in literature,[35-39] we assume that changes in the FTIR spectra could be attributed to conformational changes of the pyridinium ring and/or mesylate ion.

Despite changes observed by the FTIR and Raman spectroscopy in polymorphs A to C, the analysis of the vibrational spectroscopy didn't enable identification of the changes in subunit positions that would characterize the exact conformation of KL1421 in each polymorph. In order to identify the conformational changes in KL1421 polymorphous materials, we have used XPS spectroscopy (Fig. 4 and Table 2).

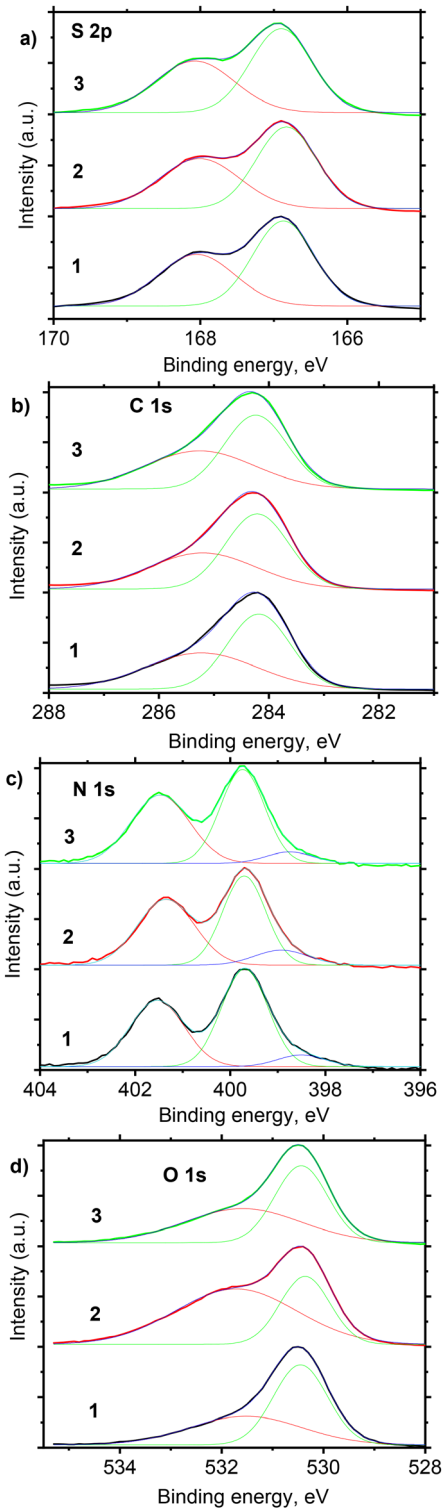

Fig. 4 Deconvoluted XPS spectra of polymorphous luminophores KL1421 A–C (1-A. 2-B, 3-C) corresponding to separate peaks: (a) S 2p (b) C 1s (c) N 1s and (d) O 1s.

XPS (X-ray photoelectron spectroscopy) analysis of polymorphic materials can reveal differences in chemical states and bonding environments due to variations in their crystal structures, leading to distinct peak positions and intensities in

Table 2 Deconvolution of XPS spectra of polymorphs A–C

	Polymorph A		Polymorph B		Polymorph C	
	BE, eV	Area	BE, eV	Area	BE, eV	Area
S 2p	168.05	0.61	168.01	0.629	168.08	0.636
	166.86	0.80	166.83	0.77	166.9	0.805
C 1s	285.23	0.85	285.20	0.823	285.26	0.890
	284.18	0.99	284.21	1.013	284.24	0.986
N 1s						
Pyridinium	401.54	0.88	401.35	0.928	401.47	0.983
Carbazole	399.7	1.114	399.70	0.945	399.74	1.02
Imine	398.51	0.136	398.92	0.198	398.75	0.131
O 1s	531.52	0.73	531.72	1.54	531.58	0.909
	530.45	0.99	530.36	0.78	530.44	0.932

XPS spectra. By analyzing these peaks, one can differentiate between polymorphs, determine their surface compositions, and gain insights into their electronic structures.

The S2p peak areas reflect changes in the position and orientation of the mesylate ion. Deconvolution of S2p XPS spectra showed two characteristic peaks with binding energies 166 eV and 168 eV, corresponding to $S2p_{3/2}$ and $S2p_{1/2}$, respectively.[25–27] In the present work, the shift of the binding energies in the mesylate counterion to lower energies has been observed, which is consistent with the deprotonated mesylate.[25–27] The calculated ratio of peak area [$S2p_{1/2}$] to peak area [$S2p_{3/2}$] was 1.31, 1.22, and 1.26 for polymorphs A, B, and C, respectively.

The analysis of XPS spectra of C 1s showed two peaks with binding energies 284.2 eV and 285.2 eV, corresponding to sp^2 (C═C) and sp^3 (C–C) bonds, respectively.[28–31] The calculated ratio of peak area [C sp^2]/[C sp^3] was 1.16, 1.24, and 1.1 for polymorphs A, B, and C, respectively. Similar to the S 2p bond, the change of orientation of the sp3 carbon between pyridinium and carbazole complexes could explain the observed changes.[25–27,32]

The analysis of XPS spectra of N 1s showed three peaks with binding energies 398.6 eV, 399.7 eV, and 401.4 eV, corresponding to imine nitrogen bonds, pyrrole-type nitrogen bonds in carbazole, and pyridinium nitrogen bonds,[33,34] respectively.[25–27,32,35] We have calculated the ratio [$N_{carbazole}/N_{pyridinium}$] and [$N_{imin}/N_{carbazole}$] for polymorphs A–C. An increase in the [$N_{carbazole}/N_{pyridinium}$] was observed from 1.01 to 1.04 and 1.22 for polymorphs B, C, and A, respectively. On the other hand, the decrease of [$N_{imin}/N_{carbazole}$] from 0.23 to 0.11 and 0.16 for polymorphs B, C, and A has been found.

The analysis of XPS spectra of O1s showed two peaks with binding energies 530.45 eV and 531.52 eV, corresponding to S═O and S–O bonds,[36] respectively.[26,27]

Changes in XPS spectra of S, O, C, and N reveal polymorphous behavior of polymorphs A–C, explained by conformational changes between carbazole and pyridinium subunits and counterion position and orientation due to dipole–dipole interactions.[26] Based on the data obtained from XRD, FTIR, Raman, and XPS measurements, we can conclude that the obtained polymorphs A, B, and C mainly differ in the relative orientation of the pyridinium ring relative to the carbazole and subsequent positioning of the mesylate counterion, to decrease dipole–dipole interactions in the conformers of the KL1421. (see Geometry calculations section) These findings are supported by previous studies of carbazole dimer packing[1,10,37] and counterion effect[11] influence on the optical properties.

3.2. Optical properties

Diffuse reflectance spectra of the polymorphs of KL1421 are shown in Fig. 5a. All polymorphs show high reflectance (80–95%) in the range of 450–800 nm. The absorption edge of KL1421 luminophores falls in the range 370–420 nm. Red shift of the absorption edge has been found from polymorph B to polymorph C and polymorph A. The observed red shift results from the change of HOMO–LUMO positions and reduction of the energy of the light, necessary for the vertical excitation of the electron from the ground state to the excited state.

In order to evaluate the observed effect in the polymorphous luminophores, we have estimated the optical band gaps of the studied polymorphs A–C. According to our previous work,[12] the diffuse reflectance is converted to absorbance by using the Kubelka–Munk equation:

$$F = \frac{(1-R)^2}{2 \cdot R} \quad (1)$$

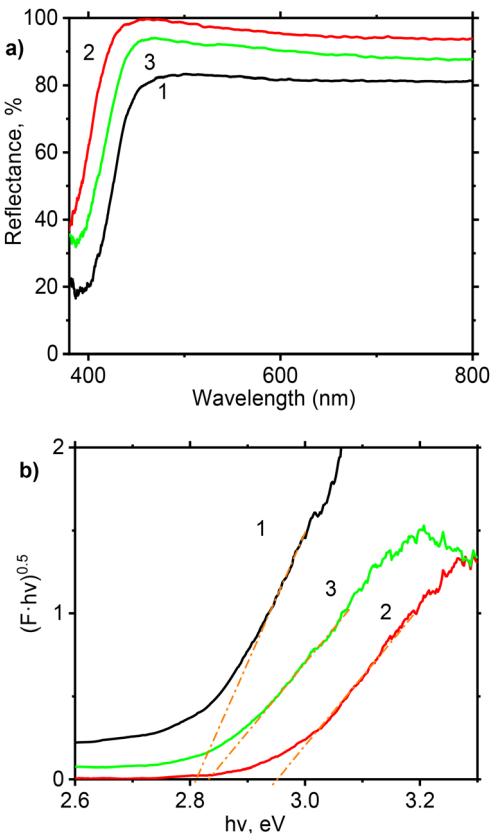

Fig. 5 Diffuse reflectance of polymorphous luminophores KL1421 A–C (1-A. 2-B, 3-C) (a) and band gap evaluation (b).

where F is the absorption coefficient, and R is the diffuse reflectance. The optical transitions can be described by the Tauc's equation:[12]

$$(F{\cdot}h\nu)^n = A{\cdot}(h\nu - E_g) \quad (2)$$

where $h\nu$, n, A, and E_g are photon energy, power coefficient (n = 1/2 or 2 for indirect and direct optical transitions, respectively), constant, and band gap energy, respectively. We have plotted equation (2) for n = 2 and n = 0.5. The linear approximation has been found only for n = 0.5 (Fig. 5b). The band gap values, graphically calculated from the absorption graph, were 2.8 eV, 2.82 eV, and 2.95 eV for polymorphs A, B, and C, respectively. Analysis of the obtained band gap values showed a significant difference (0.13–0.15 eV) in HOMO–LUMO transitions between polymorph B and polymorphs A and C.

Photoluminescence (PL) spectra of the polymorphous luminophores are presented in Fig. 6a. We observed a decrease in photoluminescence intensity and a red shift of the emission peak in polymorphs A and C compared to polymorph B.

Deconvolution of the emission profiles reveals that the broad emission band consists of two distinct electronic transitions (Fig. S1–S3 and Table S1 in SI) at 2.58 ± 0.14 eV and 2.35 ± 0.15 eV. The deconvolution results are summarized in Table 3. Deconvolution of the polymorph A PL spectrum produced two peaks at 2.56 eV and 2.32 eV. Peaks with similar positions at 2.57 eV and 2.33 eV were observed for polymorph C. While polymorph B displayed two peaks at 2.62 eV and 2.40 eV. We identified that the emission peaks of polymorph B had higher energies and integrated intensity (area).

Table 3 Deconvolution of PL spectra of polymorphs A–C

Polymorph A		Polymorph B		Polymorph C	
$h\nu$, eV	Area, μW cm^{-2}	$h\nu$, eV	Area, μW cm^{-2}	$h\nu$, eV	Area, μW cm^{-2}
2.56	1	2.62	1.03	2.57	0.98
2.32	1.59	2.40	2.01	2.33	1.72

As reported before, one of the main advantages of pyridinium luminophores is high quantum yield (QY), which is a key factor for possible optoelectronic applications of these materials.[13] KL1421 luminophore polymorphs exhibit aggregation-induced emission (AIE) with high quantum yields; the highest QY of 80% was observed for polymorph B, while polymorphs A and C displayed 61% and 69%, respectively (Fig. 6b and Table S3 in SI).

To have a better understanding of the photophysical properties of polymorphs, we analyzed the excited-state lifetimes. The averaged kinetic lifetime of the polymorphs A, B, and C are shown in Fig. 7 and Table 4. We found that emission of polymorph B, which was obtained in a slow precipitation procedure, decays as a single band with only one lifetime of 142 ns. Meanwhile, the emission of polymorphs A and C, which were obtained by swift precipitation, shows two distinct lifetime decays. For polymorph A 60 ns and 250 ns decays were recorded, while for polymorph C 113 ns and 200 ns lifetimes were recorded.

Considering the reported quantum yield values in Fig. 6b, it is possible to estimate the radiative and non-radiative decay rates of the three polymorphs as:[38]

$$\mathrm{PLQY} = \frac{k_r}{k_r + k_{nr}} \quad (3)$$

$$k_r + k_{nr} = \frac{1}{\tau} \quad (4)$$

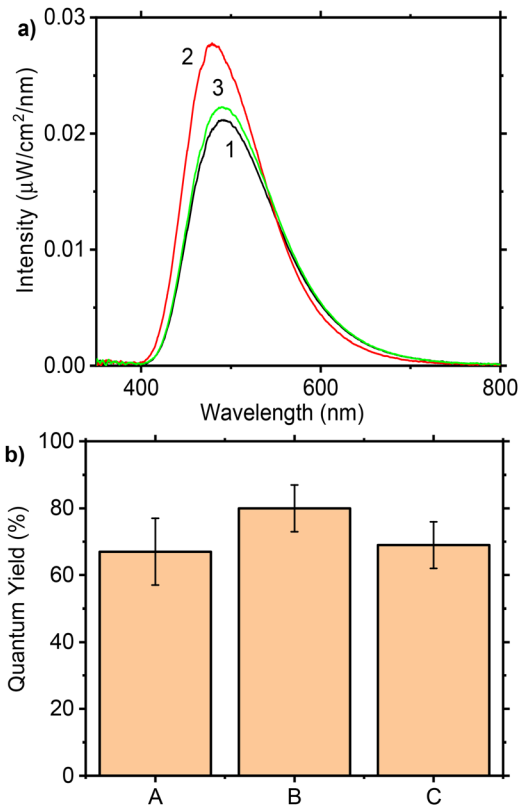

Fig. 6 Photoluminescence spectra of polymorphous luminophores KL1421 A–C (1-A. 2-B, 3-C) (a) and photoluminescence Quantum Yield values (b).

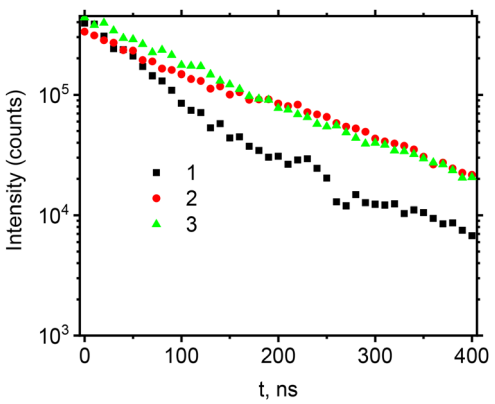

Fig. 7 Emission decay kinetics of polymorphous luminophores KL1421 A–C (1-A. 2-B, 3-C) at 500 nm (Intensity is plotted in logarithmic scale).

Table 4 Lifetime and rates of radiative and non-radiative transitions in polymorph luminophores

Polymorph	Lifetime, ns	k_r, ns^{-1}	k_{nr}, ns^{-1}
A	60 and 250	0.006	0.004
B	142	0.006	0.0014
C	113 and 200	0.005	0.002

where PLQY, k_r, k_{nr}, and τ are quantum yield, rates of radiative and non-radiative transitions, and photoluminescence lifetime, respectively. The k_r and k_{nr} rates are reported in Table 4.

A display of dual-component decay could be explained by two possible phenomena. Firstly, the swift precipitation can lead to the structural or crystalline heterogeneity of polymorphs A and C. The heterogeneity of the polymorphs could result in a trapping of two distinct structures of KL1421, which have different fluorescence lifetimes, even if the spectral shape of these two configurations is the same. The lifetime differences most likely are associated with different nonradiative transitions present in the trapped geometries. We propose that intersystem charge transfer can occur between two neighboring π^+–π^+ or π^+–π systems,[13,39] forming exciton traps. In this mechanism, before radiative relaxation, the excitons at trap sites undergo Reverse Intersystem Crossing (RISC), a process well-documented in solid-state donor–acceptor systems,[39–41] resulting in long-lived emissions. In contrast, a high degree of structural homogeneity within the crystalline lattice of polymorph B, due to a slower crystallization process, causes excitons in polymorph B undergo rapid thermalization to a single emissive minimum.

Secondly, the lifetimes of long-lived components (200 and 250 ns) are indicative of trap-assisted short Thermally Activated Delayed Fluorescence (TADF).[42] In this scenario, one of the trapped rotamers could exhibit TADF behavior due to the small singlet–triplet energy gap (ΔE_{ST} 0.004 eV), which was calculated for one of the possible structural rotamers (see Geometry calculations section and Table S4 in SI). To investigate this possibility, the temperature dependence of the photoluminescence of organic luminophores was analyzed.

The temperature dependence of polymorphous A emission is shown in Fig. 8a. The intensity of the PL spectra decreased with an increase in temperature due to an increase in non-radiative transitions, caused by the increase in vibrational contributions. The temperature dependence can be clearly observed by plotting the logarithm of photoluminescence peak intensity at 479 nm *vs.* reverse temperature (Fig. 8b). According to the literature,[43,44] the logarithm of intensity depends on temperature as:

$$\ln(I) \sim \frac{E_a}{k \cdot T} \quad (5)$$

where E_a, k, and T are the activation energy, Boltzmann's constant, and absolute temperature in Kelvin.

In the typical thermal quenching of the photoluminescence in organic luminophores, E_a is the activation energy between radiative and non-radiative transitions.[43,44] The obtained

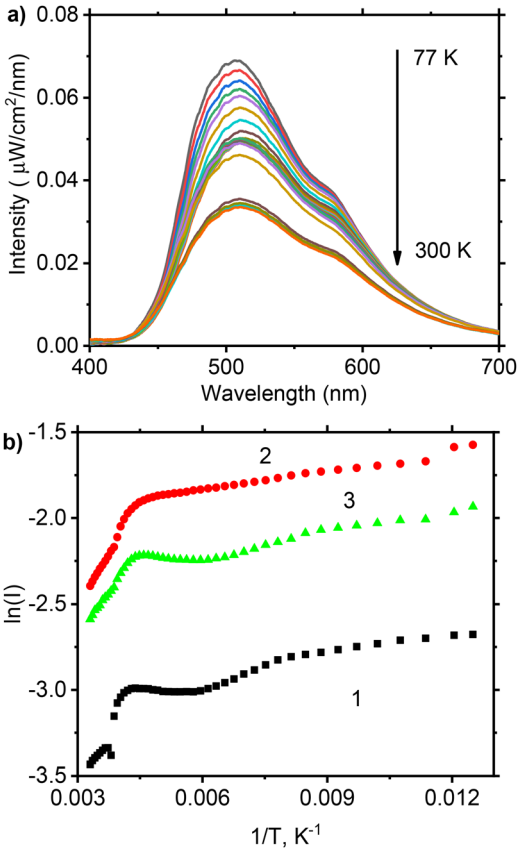

Fig. 8 Temperature dependence of the photoluminescence (Polymorph A) (a) and temperature dependence of luminescence intensity of polymorphous luminophores KL1421 A–C (1-A. 2-B, 3-C) by using, plotted at 479 nm in semi-logarithmic scale (b).

activation energies for each linear region are shown in Table 5. Interestingly, polymorphs A and C showed regions with positive and negative activation energy, whereas polymorph B displays only positive activation energy. In polymorphs A and C, a region with negative activation energies of −0.0033 eV and −0.0032 eV, respectively, was observed in the region from −100 to −30 °C. The negative linear slope of the $\ln(I)$ *vs.* $(1/T)$ and corresponding activation energy is related to the distance between the corresponding singlet and triplet states.[43,44] Negative activation energies are associated with the increase in photoluminescence with the increase in temperature. This behavior is typical of temperature-activated delayed fluorescence (TADF).[45] In the TADF, intersystem crossing from the singlet to the energetically similar triplet state

Table 5 Activation energies, calculated from the temperature dependence of photoluminescence

Polymorph A E, eV	Polymorph B E, eV	Polymorph C E, eV	T range, °C
0.0063	0.0021	0.0032	−196 to −150
		0.0089	−150 to −100
−0.0033	0.0030	−0.0032	−100 to −30
0.0355	0.0509	0.0852	−30 to 0
0.0283	0.0340	0.0206	0 to 30

occurs. From this triplet state, direct radiative relaxation is forbidden; therefore, temperature-activated reverse intersystem crossing from triplet to singlet takes place, and subsequent fluorescence is observed. The TADF process results in significantly increased photoluminescence lifetime in μs compared to the prompt fluorescence lifetime in ns.[45] According to eqn (3), the emission intensity is proportional to quantum yield. In eqn (3), the coefficient k_{nr} includes not only the thermal dissipation effects, but also electron capture to triplet states.[43,44] However, the regions of positive activation energy represent an increase in the non-radiative transitions k_{nr} with the increment of the temperature, which results in the decrease of photoluminescence intensity with the increase of temperature.

From the presented data, we can conclude that the polymorphs A and C have a temperature range from −100 to −30 °C, where a TADF behavior is observed, most likely due to a change in the pyridinium group orientation.[44,46,47] Whereas polymorph B and other temperature regions for polymorphs A and C display typical temperature-activated non-radiative transitions. Furthermore, in contrast to classical TADF, the developed KL1421 polymorphs exhibited lifetimes in the ns range because of the increase of k_{nr} with the temperature. The obtained PL data suggest that dual-decay of the polymorphs A and C is related to the heterogeneity of the crystalline structure and most likely is a function of trapped geometries, as classical TADF behavior was not observed.

3.3. Geometry calculations

In order to evaluate the influence of the luminophore geometry on the HOMO–LUMO gap, we performed optimization of KL1421 pyridinium species using b3lyp/6-31+g(d) method without any geometry restrictions. However, the mesylate counterion was omitted to simplify the calculations. The optimized structure, where pyridinium and carbazole subunits are positioned parallel to each other (a 0° twist angle, Yellow in Fig. 9), was then used as a starting point for the potential energy scan of pyridinium ring rotation with 5° increments (Fig. 9). The scan revealed the geometry of another luminophore rotamer, where the pyridinium subunit is out-of-plane relative to the carbazole subunit (Magenta in Fig. 9), featuring a donor–acceptor twist angle of 50°. Importantly, the low energy difference (1.75 kcal mol^{-1}) between the rotamers indicates that both species could be populated in a crystalline lattice. The HOMO–LUMO gap of the structure with parallel subunits (Yellow in Fig. 9) is 2.19 eV. Meanwhile, the HOMO–LUMO gap of the out-of-plane rotamer (Magenta in Fig. 9) is 2.03 eV. The higher HOMO–LUMO gap in the structure with parallel subunits (Yellow in Fig. 9) can be explained by the stabilization of the HOMO by the overlap of the electron-rich carbazole π orbital and the electron-deficient π orbital of the pyridinium subunit. At the same time, π orbitals do not overlap in the out-of-plane rotamer (Magenta in Fig. 9) due to geometric constraints, resulting in a higher HOMO and a lower HOMO–LUMO gap.[5,48,49]

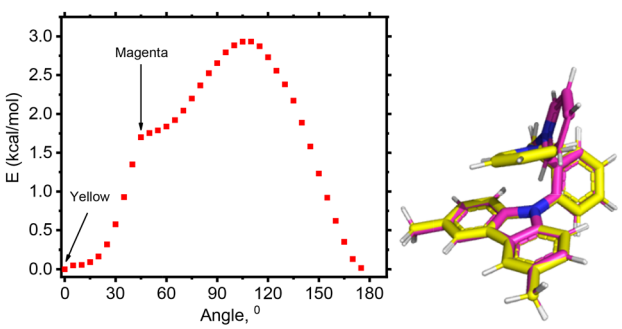

Fig. 9 Potential energy scan of pyridinium ring rotation relative to benzoyl subunit and overlay of two energetic minima.

Theoretical calculations are well aligned with experimental results. The change in orientation is significantly reflected in XRD spectra, where different crystalline planes have been detected. FTIR and Raman spectra showed a significant difference in electronic vibrations. Although many of the observed peaks remained the same, the superposition of the peaks and their intensities demonstrated the preferred vibrations as a function of molecular orientation.

This was confirmed by XPS spectroscopy. The changes observed in the XPS spectra between polymorphs A and B can be rationalized by the change in pyridinium species orientation demonstrated by the DFT calculations. This strongly indicates that the main difference between polymorphs A and B is the orientation of the pyridinium ring. Whereas XPS of polymorph C differs from polymorph A only slightly, suggesting that in this polymorph, the orientation of the pyridinium ring is similar to that of the optimized structure. Therefore, we assume that the difference between polymorphs A and C comes mainly from the position and orientation of the mesylate counterion, which was not included in the calculations.

The proposed changes in the orientation of pyridinium species significantly define the charge-transfer mechanisms. The calculated HOMO–LUMO gap difference (0.16 eV) between rotamers agrees well with the experimentally determined gap difference between polymorphs A and B (0.15 eV). Additionally, the measured negative activation energy values −0.0033 eV and −0.0032 eV, temperature-dependent luminescence in the region from −100 to −30 °C, match reasonably well with the calculated singlet–triplet gap of −0.0043 eV (See Table S4 in SI) for the out-of-plane pyridinium rotamer. Suggesting that polymorphs A and C feature an out-of-plane pyridinium rotamer, most likely as a trapped additive, while polymorph B is comprised of a lower energy rotamer with parallel pyridinium and carbazole subunits.

Based on the theoretical and experimental results, we can conclude that fabrication and transfer of KL1421 luminophores for practical applications require an optimized technical procedure. Special attention must be paid to the key parameters of KL1421-based coating preparation, such as choice of solvents, deposition, and drying conditions, to facilitate the formation of the polymorph of interest.

4. Conclusions

In this paper, we have investigated the effect of the kinetic control during the crystallization procedure on the structure and optical properties of KL1421 polymorphs.

Polymorph B exhibits a structure with parallel pyridinium and carbazole units, whereas polymorphs A and C show a heterogeneous phase combining parallel and out-of-plane pyridinium orientations. Structural and vibrational analyses revealed that variations in pyridinium orientation modify the optical properties, such as the HOMO–LUMO gap, the emission peak position, the quantum yield, and the lifetime. The temperature dependence of the photoluminescence showed a region of negative activation energy corresponding to singlet-to-triplet transitions for polymorphs A and C. Which is supported by a small singlet–triplet energy gap (−0.0043 eV) for the out-of-plane rotamer. The swift precipitation of polymorphs A and C results in heterogeneity of crystalline structure that is evident in the optical properties, as well as the two lifetimes.

Based on our previous research about their chemical stability,[12] considering the high quantum yield in the visible range, such materials could be integrated with polymeric materials to formulate UV-curable inks and electrospun luminescent nanofibers. The future research will be focused on the effect of polymers on the optical properties of KL1421. Understanding of charge transfer in KL1421-polymer structure and preservation of chemical stability and high quantum yield will be key parameters of successful transfer of KL1421 into functional coating applications.

Therefore, the significance of this study extends beyond steady-state emission tuning; it establishes a fundamental methodology to isolate and identify specific rotamers and their unique excited-state decay dynamics using kinetic crystallization control. Furthermore, our proposed approach, combining photoluminescence lifetime measurements with temperature-dependent photoluminescence, serves as an alternative, fast, and low-cost methodology for analyzing polymorphism in organic luminophores. Ultimately, this approach holds promising future perspectives for the analysis and development of composite luminescence materials, functional coatings, and smart paints.

Conflicts of interest

There are no conflicts of interest to declare.

Data availability

All experimental procedures, characterization details, and supporting data associated with this work – including the deconvolution of the photoluminescence spectrum, grouping of Raman peaks, DFT calculations, synthesis protocols, and ^{1}H NMR spectra of synthesized compounds – are available in the supplementary information (SI). See DOI: https://doi.org/10.1039/d6ma00494f.

To ensure full transparency and reproducibility, the comprehensive raw dataset supporting the findings of this study is openly available in the Zenodo repository at DOI: https://doi.org/10.5281/zenodo.18753929. This repository includes raw data files for differential scanning calorimetry (DSC), X-ray diffraction (XRD), Raman, FTIR, X-ray photoelectron spectroscopy (XPS), diffuse reflectance spectroscopy (DRS), photoluminescence (PL), temperature-dependent PL, as well as density functional theory (DFT) output files, scan energies, and ^{1}H NMR FID files.

Acknowledgements

The research is financed by the Recovery and Resilience Facility project ''Internal and External Consolidation of the University of Latvia'' (No. 5.2.1.1.i.0/2/24/I/CFLA/007) grant no. LU-BA-PA-2024/1-0040 ''Design of pyridinium luminophore structural and optical properties for tailored sensor response''. The authors gratefully acknowledge the financial support of MikroTik and the University of Latvia Foundation for the projects ''Procurement of a liquid chromatograph with a mass spectrometer detector'' and ''Acquisition of Mestrelab MNova Software for Integrated Analytical Data Processing'' implemented within the framework of the ''MikroTik project competition for the purchase of research equipment in the fields of natural, technology, and medical sciences''.

References

1 X. Xiang, Y. Zhan and F. Jin, *J. Lumin.*, 2022, **252**, 119304.
2 S. Oner and M. R. Bryce, *Mater. Chem. Front.*, 2023, **7**, 4304.
3 J. Luo, Z. Xie, J. W. Y. Lam, L. Cheng, B. Z. Tang, H. Chen, C. Qiu, H. S. Kwok, X. Zhan, Y. Liu and D. Zhu, *Chem. Commun.*, 2001, 1740.
4 X. Li, Q. Zhang and X. Zhang, *Chem. Commun.*, 2022, **58**, 104.
5 S. Kuila, H. Miranda-Salinas, J. Eng, C. Li, M. R. Bryce, T. J. Penfold and A. P. Monkman, *Nat. Commun.*, 2024, **15**, 9611.
6 K. Li, Q. Chen and P. Xue, *Tetrahedron*, 2022, **121**, 132924.
7 T. Guan, Y. Yang, Y. Liu, Z. Jiang, C. Zhuang and Y. Liu, *Ann. Phys.*, 2025, **537**, 2400253.
8 J. Ouyang, J. Chen, I. Rosbottom, W. Chen, M. Guo and J. Y. Y. Heng, *CrystEngComm*, 2021, **23**, 813.
9 M. Suresh and K. Srinivasan, *Cryst. Res. Technol.*, 2021, **56**, 2000208.
10 V. Sääsk, A. Abe, Y. Kametani, Y. Shiota, O. Sato and C. Adachi, *Chem. – Eur. J.*, 2024, **30**, e202402777.
11 K. Leduskrasts and E. Suna, *RSC Adv.*, 2020, **10**, 38107.
12 V. Zabolotnii, J. Tamuliene, M. M. Drava, T. Kirova, I. Tepliakova, V. Lukinsone, A. Kinens and R. Viter, *Appl. Mater. Today*, 2025, **46**, 102890.
13 K. Leduskrasts, A. Kinens and E. Suna, *Chem. Commun.*, 2023, **59**, 6905.
14 Y. Wang, D. Cheng, H. Zhou, J. Liu, X. Liu, Y. Wang, A. Han and C. Zhang, *Dyes Pigm.*, 2019, **170**, 107606.

15 R. A. Venditti and J. K. Gillham, *J. Appl. Polym. Sci.*, 1997, **64**, 3.
16 A. Srivastava, B. D. Joshi, P. Tandon, A. P. Ayala, A. K. Bansal and D. Grillo, *Spectrochim. Acta, Part A*, 2013, **103**, 325–332.
17 J. Srividya, V. Sivamadhavi and G. Anbalagan, *J. Mater. Sci.: Mater. Electron.*, 2022, **33**, 26522–26543.
18 D. Jesariew and M. M. Ilczyszyn, *J. Phys. Chem. Solids*, 2017, **104**, 304–314.
19 T. D. Willington, S. E. Joema, S. Sindhusha and T. C. S. Girisun, *J. Mater. Sci.: Mater. Electron.*, 2021, **32**, 25444–25461.
20 S. Jiao, W. Tang, Y. Wu, D. Li, Z. Tang, Z. Gao, X. Sun, L. Ma, H.-L. Cai and X. S. Wu, *Cryst. Growth Des.*, 2023, **23**, 2106–2119.
21 M. Akçay, *J. Mol. Struct.*, 2004, **694**, 21.
22 S. F. Parker, E. J. Revill-Hivet, D. W. Nye and M. J. Gutmann, *R. Soc. Open Sci.*, 2020, **7**, 200776.
23 N. Saghdani, A. Chihab, N. El Brahmi and S. El Kazzouli, *Molbank*, 2024, **2024**, M1858.
24 L. Pu, Y. Sun and Z. Zhang, *J. Phys. Chem. A*, 2009, **113**, 6841.
25 X.-L. Wei, M. Fahlman and A. J. Epstein, *Macromolecules*, 1999, **32**, 3114.
26 J. Landoulsi, M. J. Genet, S. Fleith, Y. Touré, I. Liascukiene, C. Méthivier and P. G. Rouxhet, *Appl. Surf. Sci.*, 2016, **383**, 71.
27 X. Zhang, J. Wang, Y. Liu, Y. Hao, F. Yu, D. Li, X. Huang, L. Yu, T. Wang and H. Hao, *J. Phys. Chem. C*, 2021, **125**, 6189.
28 S. O. Ganiyu, M. J. G. De Araújo, E. C. T. De Araújo Costa, J. E. L. Santos, E. V. Dos Santos, C. A. Martínez-Huitle and S. B. C. Pergher, *Appl. Catal., B*, 2021, **283**, 119652.
29 M. Skorupska, P. Kamedulski, J. P. Lukaszewicz and A. Ilnicka, *Nanomaterials*, 2021, **11**, 760.
30 J. S. Stevens, A. C. De Luca, M. Pelendritis, G. Terenghi, S. Downes and S. L. M. Schroeder, *Surf. Interface Anal.*, 2013, **45**, 1238.
31 C. Tang, J. Zhu, Q. Zhou, J. Wei, R. Zhu and H. He, *J. Phys. Chem. C*, 2014, **118**, 26249.
32 J. Zeng, Z. Tang, J. Yin, Z. Guan, R. Wei, X. Ke and X. Liu, *Chem. Eng. J.*, 2024, **502**, 157819.
33 C.-X. Liu, S. Hwang, Y. Lee, Y. H. Ko, S. S. Park and E. Lee, *ACS Appl. Mater. Interfaces*, 2024, **16**, 48203.
34 H. Wang, D. Wu, K. Chen, N. Gu, Y. Chen and B. Zhang, *ACS Mater. Lett.*, 2024, **6**, 3376.
35 D. Barman, D. Barman, K. Bhattacharyya and P. K. Iyer, *Adv. Opt. Mater.*, 2024, **12**, 2401352.
36 M. M. Nasef and H. Saidi, *Appl. Surf. Sci.*, 2006, **252**, 3073.
37 K. Lee and D. Kim, *Int. J. Quantum Chem.*, 2020, **120**, e26363.
38 S. Sem, S. Jenatsch, K. Stavrou, A. Danos, A. P. Monkman and B. Ruhstaller, *J. Mater. Chem. C*, 2022, **10**, 4878.
39 K. Leduskrasts and E. Suna, *RSC Adv.*, 2019, **9**, 460–465.
40 P. L. dos Santos, F. B. Dias and A. P. Monkman, *J. Phys. Chem. C*, 2016, **120**, 18259–18267.
41 T. J. Penfold and J. Eng, *ChemPhotoChem*, 2023, **7**, e202200243.
42 C. Adachi and A. S. D. Sandanayaka, *CCS Chem.*, 2020, **2**, 1203–1216.
43 S. Guha, J. D. Rice, Y. T. Yau, C. M. Martin, M. Chandrasekhar, H. R. Chandrasekhar, R. Guentner, P. Scanduicci De Freitas and U. Scherf, *Phys. Rev. B: Condens. Matter Mater. Phys.*, 2003, **67**, 125204.
44 N. Haase, A. Danos, C. Pflumm, A. Morherr, P. Stachelek, A. Mekic, W. Brütting and A. P. Monkman, *J. Phys. Chem. C*, 2018, **122**, 29173.
45 H. Uoyama, K. Goushi, K. Shizu, H. Nomura and C. Adachi, *Nature*, 2012, **492**, 234–238.
46 Y. Zeng, X. Zhai, G. Wang, Y. Su, M. Wu, B. Wang and K. Zhang, *Dyes Pigm.*, 2023, **219**, 111643.
47 Q. Peng, D. Fan, R. Duan, Y. Yi, Y. Niu, D. Wang and Z. Shuai, *J. Phys. Chem. C*, 2017, **121**, 13448.
48 R. M. Williams, *Photochem. Photobiol. Sci.*, 2010, **9**, 1018.
49 L. V. Brownell, K. A. Robins, Y. Jeong, Y. Lee and D.-C. Lee, *J. Phys. Chem. C*, 2013, **117**, 25236.